

Retrieval of Surface Spectral Emissivity in Polar Regions based on the Optimal Estimation Method

Yan Xie¹, Xianglei Huang^{1*}, Xiuhong Chen¹, Tristan S. L'Ecuyer², Brian J. Drouin³, Jun Wang⁴

¹Department of Climate and Space Sciences and Engineering, University of Michigan, Ann Arbor, Michigan.

²Department of Atmospheric and Oceanic Sciences, University of Wisconsin-Madison, Madison, WI.

³Jet Propulsion Laboratory, California Institute of Technology, Pasadena, CA.

⁴Department of Chemical and Biochemical Engineering, University of Iowa, Iowa City, IA.

* Corresponding author: Xianglei Huang, Department of Climate and Space Sciences and Engineering, University of Michigan, Ann Arbor, Michigan 48109-2143, United States.
xianglei@umich.edu, +1-734-936-0491.

Original Submission on August 9, 2021

Revision on December 28, 2021

This is the author manuscript accepted for publication and has undergone full peer review but has not been through the copyediting, typesetting, pagination and proofreading process, which may lead to differences between this version and the [Version of Record](#). Please cite this article as [doi: 10.1029/2021JD035677](https://doi.org/10.1029/2021JD035677).

This article is protected by copyright. All rights reserved.

Key Points:

- An optimal-estimation algorithm for surface spectral emissivity retrieval is developed and assessed for the forthcoming PREFIRE mission.
- Surface spectral emissivity retrievals in the far-infrared can be significantly influenced by the atmospheric water vapor abundance.
- Compared to the mid-infrared, the far-infrared surface emissivity retrievals are more affected by the choice of *a priori* constraints.

Abstract

Surface spectral emissivity plays an important role in the polar radiation budget. The significance of surface emissivity in the far-infrared (far-IR) has been recognized by recent studies, yet there have been no observations to constrain far-IR surface spectral emissivity over the entire polar regions. In preparation for the Polar Radiant Energy in the Far-InfraRed Experiment (PREFIRE) mission, this study develops and assesses an optimal estimation-based retrieval algorithm to estimate both mid-IR and far-IR polar surface emissivity from the future PREFIRE measurements. Synthetic PREFIRE spectra are simulated by feeding the ERA5 reanalysis and a global surface emissivity dataset to a radiative transfer model. Information content analysis indicates that the far-IR surface emissivity retrievals can be more influenced by the atmospheric water vapor abundance than the mid-IR counterparts. When the total column water vapor is above 1cm, the far-IR surface emissivity retrievals largely rely on the *a priori* constraints. Performance of the optimal-estimation algorithm is assessed using 960 synthetic PREFIRE clear-sky radiance spectra over the Arctic. The results based on current best estimate of instrument performance show that all retrievals converge within 15 iterations, the retrieved surface spectral emissivity has a mean bias within ± 0.01 and a root-mean-square error less than 0.024. The far-IR surface emissivity retrievals are much more affected by the *a priori* choice than the mid-IR ones. A properly constructed *a priori* covariance can also help to improve the computational efficiency. Influences of other factors for future operational retrievals are also discussed.

1. Introduction

Surface emissivity is defined as the ratio of actual surface thermal emission to the radiation of a blackbody with the same temperature as the surface. It is a spectrally dependent property of surface composition that directly affects surface upward thermal emission and reflection of atmospheric downward thermal radiation at the surface, thus playing an important role in the radiation budget of the climate system. In addition, surface emissivity is also a key quantity to observe in remote sensing, for its inseparable role in atmospheric sounding (Li et al., 2007; Zhou et al., 2011; Capelle et al., 2012; Smith & Barnet, 2019), in the monitoring of surface compositions of rocky planets (Christensen et al., 2001; Rockwell & Hofstra, 2008), land cover changes (French et al., 2008; Hulley et al., 2015), evaporative stress indices (Fisher et al., 2020), and remote sensing of fires (Peterson and Wang, 2013). As a result, mid-infrared (mid-IR, 5 to 15 μm) surface emissivities, especially those over the mid-IR window regions, have become routine retrieval products from spaceborne multi-spectral imagers and infrared hyperspectral sounders such as Advanced Spaceborne Thermal Emission and Reflection Radiometer (ASTER) (Gillespie et al., 1998), Moderate Resolution Imaging Spectroradiometer (MODIS) (Wan & Li, 1997), Atmospheric Infrared Sounder (AIRS) (Susskind et al., 2003), and Infrared Atmospheric Sounding Interferometer (IASI) (Schlüssel et al., 2005).

While the aforementioned observations only provide information about mid-IR surface spectral emissivity, the importance of far-IR (15 to 100 μm) surface emissivity to polar climate has been recognized in recent years. For example, Chen et al. (2014) used theoretically calculated far-IR spectral emissivity of several snow surfaces to show non-negligible bias in radiation budget when such surfaces are assumed to be blackbody instead. Feldman et al. (2014) demonstrated that different specifications of surface spectral emissivity in a climate model could

cause noticeable changes in the simulated polar surface climatology. Huang et al. (2018) incorporated a global surface spectral emissivity database, which was developed in Huang et al. (2016), into the NCAR Community Earth System Model 1.1.1 and showed statistically significant differences in the simulated long-term mean polar surface temperature and sea ice content. Huang et al. (2018) further evaluated surface emissivity feedback in response to the doubling of CO₂ and concluded that such surface emissivity feedback is smaller than the surface albedo feedback by at least one order of magnitude. These studies have directly motivated observational efforts to measure and monitor far-IR surface spectral emissivity, especially in the polar regions, which then encouraged the selections of two satellite missions dedicated to far-IR observations, i.e., PREFIRE (Polar Radiant Energy in the Far InfraRed Experiment; L'Ecuyer et al., 2021) by NASA and FORUM (Far-infrared Outgoing Radiation Understanding and Monitoring; Palchetti et al., 2020) by ESA.

Surface emissivity retrievals in the far-IR usually face more challenges than in the mid-IR due to the strong interference of water vapor absorption. Channels used in the mid-IR surface emissivity retrievals are always transparent for clear-sky situations. Even for the most humid scenes on the earth when the total column water vapor (TCWV) is around 9 cm, the clear-sky transmittances over mid-IR window channels are no less than 0.8. In contrast, the entire far-IR band becomes nearly opaque (transmittance < 0.05) once the TCWV exceeds 1 cm (Feldman et al., 2014). As a reference, based on ERA-5 reanalysis climatology from 2001 to 2020, the global mean TCWV is approximately 2.5 cm, while that over the Arctic and Antarctic is 0.8 cm and 0.4 cm (Figure 5), respectively. These facts imply that far-IR surface emissivity can only be inferred from space-borne observations over polar or high-elevation regions where the TCWV is small enough.

There have been no space-borne far-IR observations since the pioneering measurements by Infrared Interferometer Sounder-D (IRIS-D) aboard the *Nimbus IV* (Hanel et al., 1971), which measured nadir-view outgoing spectral radiances from 6.25 to 25 μm with a footprint of 94 km in diameter from April 1970 to January 1971. Efforts in retrieving far-IR surface emissivity have been limited by the scarcity of spectral observations except for a few field campaigns in recent years. Bellisario et al. (2017) retrieved far-IR surface emissivity from spectral observations made by the TAFTS (Tropospheric Airborne Fourier Transform Spectrometer; Canas et al., 1997), a Fourier interferometer with spectral coverage of 17-125 μm . The measurements were done from an aircraft over a limited region of the Greenland Plateau in March 2015. They retrieved far-IR surface spectral emissivity from 18.7 to 125 μm and highlighted the need for further research on the simultaneous retrievals of mid-IR and far-IR surface emissivities. Murray et al. (2020) adopted the retrieval framework in Bellisario et al. (2017) and validated the feasibility of retrieving mid-IR and far-IR surface emissivity from the TAFTS spectra measured at a higher altitude than those in Bellisario et al. (2017). Furthermore, Murray et al. (2020) also confirmed the theoretical calculations in Chen et al. (2014) and Huang et al. (2016) by demonstrating that the far-IR emissivities of snow and ice surfaces can be significantly less than unity, especially over the so-called far-IR dirty window (16.7 to 25 μm) (Rathke et al., 2002). These two studies were restricted to observations in March 2015 over a limited region in the Greenland Plateau. The PREFIRE mission, on the other hand, aims to measure in both mid-IR and far-IR (5 to 45 μm , with a resolution of 0.84 μm) over polar regions at hourly to seasonal scales for the first time (L'Ecuyer et al., 2021). PREFIRE will provide an unprecedented opportunity in this decade for retrievals of far-IR surface emissivity in the polar regions. Thus, it is necessary to develop retrieval algorithms in preparation for such future observations.

Many algorithms have been developed for the retrieval of surface spectral emissivity and can be generally categorized as either statistical methods or physical methods (Kidder et al., 1995). Statistical methods make use of empirical relationships or auxiliary assumptions to constrain the retrieval problem (Li et al., 2013). Several widely used statistical methods for mid-IR surface emissivity retrievals are the Normalized Emissivity Method (Gillespie, 1986), the Temperature-Emissivity Separation Methods (Gillespie et al., 1998; Hulley et al., 2018), and the Temperature Independent Spectral Indices Method (Becker & Li, 1990a). For these statistical methods, the training of empirical coefficients strongly depends on the accuracy of atmospheric corrections (Coll et al., 2003) and can vary with geographical regions. Split-window retrieval is another widely used statistical method, which assumes a linear relationship between surface temperature and brightness temperatures in mid-IR adjacent window channels (Price, 1984). This linear approximation is valid in the mid-IR window region due to the weak clear-sky atmospheric attenuation (Becker & Li, 1990b), yet cannot hold true anymore in the far-IR where water vapor absorption tends to be strong. Physical methods, on the other hand, require fewer empirical assumptions than the statistical methods: surface spectral emissivities are iteratively retrieved by minimizing differences between the forward radiative transfer calculations and actual measurements with the observational uncertainty taken into account. The optimal estimation (OE) method is a representative physical method, which combines *a priori* knowledge and observations based on the Bayesian framework to generate the retrieval results (Rodgers, 1976). The OE method has been widely adopted in retrieval studies and has shown satisfactory performance for the retrievals of atmospheric profiles (Turner & Löhnert, 2014; Maahn et al., 2020), precipitation (L'Ecuyer and Stephens, 2002; Wood and L'Ecuyer, 2021), and surface parameters such as surface temperature, sea ice concentration (Scarlat et al., 2017) as well as

mid-IR surface emissivity (Liu et al., 2009; Divakarla et al., 2014). Such success of OE retrievals in the mid-IR motivates us to use it for the inversion of the far-IR surface spectral emissivity.

This study implements the OE method to retrieve surface spectral emissivity in both the mid-IR and far-IR, and assess the retrieval performance based on the synthetic PREFIRE radiances in the polar regions. Section 2 introduces the data and the forward modeling tool used in the study. Section 3 describes the relevant technical details of the OE retrieval algorithm. The analysis of information content and retrieval results are presented in Section 4, followed by further discussions and conclusions in Section 5.

2. Data and Forward Modeling

2.1 ERA5 reanalysis data

The ERA5 reanalysis is the latest atmospheric reanalysis produced by the European Centre for Medium-Range Weather Forecasts (ECMWF) (Hersbach et al., 2020). The ERA5 reanalysis is based on the Integrated Forecasting System (IFS) Cy41r2 with a 4-D variational data assimilation scheme. Hersbach et al. (2020) also show that the ERA5 is superior to the precedent ERA-Interim reanalysis (Dee et al., 2011). The ERA5 has a horizontal resolution of 0.25°-by-0.25° and a vertical coverage of 37 pressure levels up to 1 hPa. It provides hourly outputs as well as monthly means of essential atmospheric and surface variables.

2.2 Global surface spectral emissivity dataset used in the simulation

An observationally based global surface spectral emissivity dataset at 0.5°-by-0.5° spatial resolution has been developed by Huang et al. (2016) over the entire longwave spectrum for a variety of surface types, such as water, snow (fine, medium, and coarse grains), ice and tundra which are typical in the polar regions. This dataset is based on a set of first-principle calculations

as well as the mid-IR surface spectral emissivity retrievals from the MODIS measurements (Seemann et al., 2008) at 0.05°-by-0.05° resolution. Huang et al. (2016) validated the mid-IR part of the dataset against surface spectral emissivity retrievals from IASI observations (Zhou et al., 2011). It has been demonstrated that the global-mean surface emissivity differences between this dataset and the IASI retrievals are within ± 0.006 for four mid-IR bands from 820 to 1800 cm^{-1} (12.2 to 5.6 μm) and the relevant root-mean-square (RMS) differences are less than 0.026 in both January and July (Huang et al., 2016). As there have been no far-IR measurements of surface spectral emissivity to validate the dataset, the far-IR surface emissivities in Huang et al. (2016) are based on either first-principle calculations (for snow, ice, desert, water, etc.) or extrapolation from the mid-IR counterparts (for vegetation surface types). More details about this dataset can be found in Huang et al. (2016). This dataset is used in our study for the simulation.

Additionally, the *a priori* covariance matrix of surface spectral emissivities in the retrieval scheme is also constructed from this dataset. The nonexistence of any observed far-IR surface emissivity dataset leaves no choice but constructing *a priori* covariance matrix in this way.

2.3 PCRTM forward model in the retrieval scheme

A radiative transfer model is essential to physical retrievals. The Principal Component-based Radiative Transfer Model (PCRTM) V3.4 (Liu et al., 2006) is used to compute clear-sky radiances and Jacobians at the PREFIRE channels. Compared to the benchmark line-by-line radiative transfer calculations, the PCRTM makes use of correlations between spectral channels to predict the scores of precomputed principal components and greatly reduces the computational burden without significant loss of accuracy. Liu et al. (2006) demonstrated that, compared to the benchmark calculation, the root-mean-square error (RMSE) of the PCRTM calculation can be less than 0.4 K in brightness temperature. Chen et al. (2013) showed that the RMSE between the

PCRTM V2.1 and the LBLRTM (Line-By-Line Radiative Transfer Model) 12.0 (Clough et al., 2005) in brightness temperature was 0.67 K for a random clear-sky profile, and the PCRTM was approximately 4480 times faster than the LBLRTM. More details about the PCRTM can be found in Liu et al. (2006). Chen et al. (2013) also developed a PCRTM-based simulator that can conveniently interface with reanalysis profiles and has been subsequently used in several studies (Huang et al., 2014; Bantges et al., 2016; Pan et al., 2017; Chen et al., 2018). This PCRTM-based simulator is also used in this study as the forward model in the retrieval scheme.

2.4 The PREFIRE mission: relevant design and current estimates of the noise level

The PREFIRE mission, scheduled to launch no earlier than December 2022, will employ two CubeSats to operate in near-polar orbits (82°-98° inclination) and collect observations of polar spectral emission in both mid-IR and far-IR on hourly to seasonal timescales (L'Ecuyer et al., 2021). Each spacecraft will carry a Thermal InfraRed Spectrometer (TIRS), a grating spectrometer with 64 channels covering 0-54 μm at a spectral resolution of 0.84 μm and a field of view comparable to AIRS (L'Ecuyer et al., 2021). TIRS will record spectral radiances over eight cross-track pixels, all within near nadir view. The manufacturing and assembling of TIRS instruments are ongoing. For brevity, hereafter PREFIRE will be used interchangeably with the PREFIRE TIRS instrument. The current best estimates of the noise equivalent spectral radiances (NeSRs) for PREFIRE channels in the mid-IR window and far-IR dirty window regions are shown in Figure 1a. These current estimates of NeSRs are used in our study to estimate measurement noises at each channel (i.e., Gaussian noise with the standard deviation being the estimated NeSR). Noises at different channels are assumed to be independent from each other. The PREFIRE TIRS is a push-broom device, intended to make eight cross-track measurements with each footprint around 10 km in diameter and viewing zenith angle θ within $\pm 10^\circ$ (i.e.,

$\cos\theta \geq 0.985$). Given such small deviation from nadir view, here we examine only the nadir-view geometry. The dependence of viewing zenith angle will be considered in the actual retrieval.

2.5 Forward modeling strategy and selection of PREFIRE channels

Two sets of simulations are carried out using the aforementioned PCRTM simulator and ERA5 reanalysis profiles. The first set is for an overall evaluation of the degree of freedoms (DoFs) and averaging kernels for the surface emissivity retrievals. And the second set is generated for assessment of the retrieval algorithm performance. Two polar regions featured with very different total column water vapor (TCWV) are chosen for the first set of simulations, namely, mid-Arctic Ocean (73-77°N, 0-360°E) and Antarctic Plateau (75-85°S, 60-90°E). The ERA5 climatological mean profiles averaged from 2001-2020 over each region are used to compute the DoFs and averaging kernel matrices. Given the seasonal variation of TCWV, such calculation is made for January and July, respectively.

For the second set of simulations, 240 ERA5 hourly profiles are selected from the Arctic region (60-90°N, 0-360°E), with equal separation both spatially and temporally, in each month of January, April, July, and October 2005, i.e., 960 profiles in total. As to be illustrated in the following section, TCWV affects the DoFs for surface emissivity retrievals the most. In general, the Arctic has a larger TCWV than the Antarctic. Therefore, the retrieval algorithm can be evaluated over a wider range of conditions in the Arctic than in the Antarctic. The ERA5 vertical profiles of temperature and humidity, as well as its surface skin temperatures and surface pressures are fed into the PCRTM simulator. Surface spectral emissivities used in the forward modeling are from Huang et al. (2016) over the same location as the individual ERA5 profiles, but perturbed with a uniformly distributed random number between -0.05 and 0.05. If the perturbed emissivity at a given frequency happens to be larger than one, it is then reset to 0.98.

These perturbed surface emissivities are necessary for the retrieval assessment, as it makes the (modeled) true surface emissivities not exactly the same as those used in constructing the *a priori* covariance. By doing so, the PCRTM simulator can provide the clear-sky TOA (top-of-the-atmosphere) radiances at 1cm^{-1} spectral resolution from 50 to 2760 cm^{-1} (i.e., 200 to $3.6\text{ }\mu\text{m}$). Such PCRTM spectra are then convolved with the PREFIRE spectral response functions (SRFs) to generate synthetic PREFIRE clear-sky radiances (as examples, SRFs of one mid-IR and one far-IR channels are shown in Figure 1c and 1d, respectively). Figure 1b shows two examples of such synthetic clear-sky radiances at the PREFIRE channels in the mid-IR window and far-IR dirty window, one for the mid-Arctic Ocean in the boreal winter and the other for the Antarctic Plateau in the austral winter. To mimic the realistic observations, Gaussian random noises based on the NeSRs shown in Figure 1a are added to the synthetic PREFIRE radiances. Both synthetic clear-sky radiances with and without measurement noises are used in the following sections.

Not all PREFIRE channels are suitable for the surface emissivity retrievals. For the far-IR channels outside of the dirty window region (i.e., wavelength $> 25\mu\text{m}$), water vapor absorption is always strong even when $\text{TCWV} < 0.1\text{ cm}$ (Feldman et al, 2014), leading to little sensitivity to surface emission all over the polar regions. Thus, such channels are not used in our retrievals.

One PREFIRE channel centered at $9.28\text{ }\mu\text{m}$ falls in the O_3 $9.6\text{ }\mu\text{m}$ band, so it is excluded to avoid the complexity of modeling O_3 profiles. For the remaining PREFIRE channels in the mid-IR window, mid-IR CO_2 band, and far-IR dirty window regions, we further scrutinize their clear-sky transmittances in the mid-Arctic Ocean and Antarctic Plateau for January and July, as shown in Figure 1e and 1f, respectively. The clear-sky transmittances of mid-IR window channels from $8.4\text{ }\mu\text{m}$ to $12.7\text{ }\mu\text{m}$ are all above 0.6 with small variations from winter to summer. The channel centered on $13.5\text{ }\mu\text{m}$ sits in the wing of CO_2 band and has a clear-sky transmittance of no less

than 0.3 in the mid-Arctic Ocean and larger than 0.6 in Antarctic Plateau for both seasons, suggesting non-negligible sensitivity to the surface emission. Thus, six mid-IR channels from 8.4 μm to 13.5 μm (PREFIRE channel No. 10 and 12-16) are chosen for the surface emissivity retrievals. As for channels in the far-IR dirty window, the clear-sky transmittances exhibit much larger variations with TCWV than their mid-IR counterparts. For example, the clear-sky transmittance at 18.6 μm in the mid-Arctic Ocean drops from 0.47 in January to 0.09 in July. Over the Antarctic Plateau, it only decreases from 0.91 in July to 0.79 in January. Therefore, it can be expected that retrieving surface emissivity over such far-IR dirty window channels is more challenging for the Arctic Ocean than for the Antarctic Plateau. As a compromise, we choose eight channels in the far-IR from 16.9 μm to 22.8 μm (PREFIRE channel No. 20-27) for the surface emissivity retrievals. All eight channels have clear-sky transmittances above 0.6 over the Antarctic Plateau and larger than 0.16 over the Arctic Ocean in January. In total, fourteen PREFIRE channels are chosen for the surface emissivity retrievals. More details about the selected channels can be found in Table 1.

3. Retrieval methodology

The retrieval method adopted here largely follows the optimal estimation retrieval framework depicted in Rodgers (2000). Below is a brief depiction of the method and how to construct the *a priori* covariance matrix for our retrieval algorithm.

3.1 Optimal estimation method

The radiance observations made at the TOA, denoted by \mathbf{y} , contain both outgoing radiances originated from the climate system and measurement noise. To mimic this fact, as mentioned

above, each synthetic PREFIRE radiance consists of the spectral radiance from the PCRTM given an input state vector \mathbf{x} , denoted as $F(\mathbf{x})$, and the measurement noise ϵ .

$$\mathbf{y} = F(\mathbf{x}) + \epsilon \quad (1)$$

Following the notation used in Rodgers (2000), $P(\mathbf{x})$ denotes the *a priori* probability distribution of the state vector \mathbf{x} , and $P(\mathbf{x}|\mathbf{y})$ denotes the *a posteriori* probability of \mathbf{x} given the observation \mathbf{y} .

Assuming Gaussian distributions for both the likelihood $P(\mathbf{y}|\mathbf{x})$ and the *a priori* $P(\mathbf{x})$, $P(\mathbf{x}|\mathbf{y})$ then also follows a Gaussian distribution. The optimal estimation retrieval method seeks a solution, $\hat{\mathbf{x}}$, which maximizes the *a posteriori* probability $P(\mathbf{x}|\mathbf{y})$. $\hat{\mathbf{S}}$ denotes the *a posteriori* covariance matrix and evaluates the retrieval uncertainty of $\hat{\mathbf{x}}$. Solutions of $\hat{\mathbf{x}}$ and $\hat{\mathbf{S}}$ can be expressed as

$$\hat{\mathbf{x}} = (\mathbf{K}^T \mathbf{S}_\epsilon^{-1} \mathbf{K} + \mathbf{S}_a^{-1})^{-1} (\mathbf{K}^T \mathbf{S}_\epsilon^{-1} \mathbf{y} + \mathbf{S}_a^{-1} \mathbf{x}_a) \quad (2)$$

$$\hat{\mathbf{S}} = (\mathbf{K}^T \mathbf{S}_\epsilon^{-1} \mathbf{K} + \mathbf{S}_a^{-1})^{-1} \quad (3)$$

where \mathbf{x}_a and \mathbf{S}_a are the *a priori* mean and covariance matrix of \mathbf{x} , which represent the knowledge of state variables before the observations, \mathbf{S}_ϵ is the noise covariance matrix that, in the context of information content analysis from satellite measurement, normally consider both the instrument noises and forward model errors (Xu et al., 2018), and $\mathbf{K} = \partial F(\mathbf{x})/\partial \mathbf{x}$ is the Jacobian matrix. The optimal estimate $\hat{\mathbf{x}}$ can be viewed as a sum of *a priori* mean and observed signal weighted by the inverse of covariance matrices. For moderately linear cases where the second-and higher-order derivative terms are negligible, $\hat{\mathbf{x}}$ can be obtained by using the iterative Gauss-Newton method to find the root of $\nabla_{\mathbf{x}}[-\ln(P(\mathbf{x}|\mathbf{y}))] = 0$. Estimated $\hat{\mathbf{x}}$ at the (i+1)-th iteration step, \mathbf{x}_{i+1} , can be expressed as

$$\mathbf{x}_{i+1} = \mathbf{x}_a + (\gamma \mathbf{S}_a^{-1} + \mathbf{K}_i^T \mathbf{S}_\epsilon^{-1} \mathbf{K}_i)^{-1} \mathbf{K}_i^T \mathbf{S}_\epsilon^{-1} [\mathbf{y} - F(\mathbf{x}_i) + \mathbf{K}_i(\mathbf{x}_i - \mathbf{x}_a)] \quad (4)$$

where \mathbf{x}_i and \mathbf{K}_i are the estimates of $\hat{\mathbf{x}}$ and its Jacobian at the i -th iteration, respectively.

Corresponding, the estimated $\hat{\mathbf{S}}$ at the i -th iteration can be written as

$$\mathbf{S}_i = (\gamma \mathbf{S}_a^{-1} + \mathbf{K}_i^T \mathbf{S}_\epsilon^{-1} \mathbf{K}_i)^{-1} (\gamma^2 \mathbf{S}_a^{-1} + \mathbf{K}_i^T \mathbf{S}_\epsilon^{-1} \mathbf{K}_i) (\gamma \mathbf{S}_a^{-1} + \mathbf{K}_i^T \mathbf{S}_\epsilon^{-1} \mathbf{K}_i)^{-1} \quad (5)$$

Different from the formulas in Rodgers (2000), a tuning parameter γ is introduced in Equations (4) and (5) to manually adjust the relative weight of *a priori* constraints and observed information (Carissimo et al., 2005; Zhou et al., 2007; Masiello et al., 2012; Turner & Löhnert, 2014). This modification is meant to stabilize the retrieval process by gradually adding information from the observations step by step. Following the work of Turner and Löhnert (2014), a sequence of γ values [1000, 300, 100, 30, 10, 3, 1, 1, 1, \dots , 1] has been used in this study. The iteration stops when $\gamma = 1$ and the following convergence criterion is met.

$$(\mathbf{x}_i - \mathbf{x}_{i+1})^T \mathbf{S}_i^{-1} (\mathbf{x}_i - \mathbf{x}_{i+1}) < \frac{\text{length}(\mathbf{x})}{10} \quad (6)$$

This convergence criterion assures that the change of \mathbf{x} between two consecutive iterations is smaller than the retrieval uncertainty by at least an order of magnitude.

3.2 Construction of *a priori* covariance matrix \mathbf{S}_a

Among all the terms describes in Equations (1)-(6), \mathbf{K} is straightforward to obtain directly from the PCRTM, and \mathbf{S}_ϵ is a diagonal matrix which assumed to be decided by the NeSRs (since the forward model errors are unknown given the scarcity of the measurements in the far IR). On the other hand, \mathbf{x}_a and \mathbf{S}_a are specified in a more subjective way than \mathbf{K} and \mathbf{S}_ϵ .

A priori knowledge of \mathbf{x} can be obtained from climatological data, laboratory measurements or empirical analysis. In this study, the *a priori* mean \mathbf{x}_a of surface spectral emissivity are set to 0.95. The *a priori* covariance matrix \mathbf{S}_a is derived from the global surface emissivity database (Huang et al., 2016) described in Section 2.2. Specifically, nadir-view surface spectral emissivity

from Huang et al. (2016) is first averaged onto each PREFIRE channel, and then a covariance matrix is computed from such surface emissivity data at the PREFIRE spectral resolution. Since there have been no measurements available to validate the far-IR surface emissivity in Huang et al. (2016), we decide not to directly use the computed covariance matrix as \mathbf{S}_a . Two further adjustments are made instead: (1) doubling the *a priori* uncertainty of surface emissivity as derived from Huang et al. (2016) for each PREFIRE channel so that the tolerable range of surface emissivity at each PREFIRE channel becomes larger; (2) halving the linear correlation coefficients between the surface emissivities of two channels as derived from Huang et al. (2016), so that the retrievals of surface spectral emissivity can be less affected by the inter-channel correlation. \mathbf{S}_a constructed in this way is shown in Figure 2. The variance in the mid-IR window channels (channels 10, 12-14) is around 10^{-4} , much smaller than the variance in the rest channels ($\sim 8.3 \times 10^{-4} - 1.4 \times 10^{-3}$). The covariance of surface emissivities between two far-IR channels is positive and the covariance between one far-IR and one mid-IR channel is in general negative, but the latter one is much smaller in magnitude than the former one.

4. Results

4.1 Information content analysis

The information content analysis provides an estimate of how much information contributed by the true surface spectral emissivity can be captured by the observations given the specified NeSRs and the *a priori* knowledge. Different metrics have been developed to evaluate the information content, such as the Fisher information matrix (Fisher, 1922), the Shannon information matrix (Shannon & Weaver, 1949), the averaging kernel matrix (Backus et al., 1970), and the degree of freedom (DoF) for signal (Rodgers, 2000). Here the averaging kernel

and the DoF will be used in the information content analysis for two different polar topographical regions, the mid-Arctic Ocean (73-77°N, 0-360°E) and Antarctic Plateau (75-85°S, 60-90°E with an averaged elevation ~3.2km). The ERA5 climatological monthly mean profiles in January and July from 2001 to 2020 over each region are used in the analysis.

The averaging kernel matrix, \mathbf{A} , quantitatively evaluates the sensitivity of retrieval results to the true surface emissivity. It can be expressed as

$$\mathbf{A} = \frac{\partial \hat{\mathbf{x}}}{\partial \mathbf{x}} = \mathbf{S}_a \mathbf{K}^T (\mathbf{K} \mathbf{S}_a \mathbf{K}^T + \mathbf{S}_\epsilon)^{-1} \mathbf{K} \quad (7)$$

In our case, the rows of \mathbf{A} represent the sensitivity of retrieved surface emissivity at a given channel to the true surface emissivity at all fourteen selected channels. The diagonal elements denote the sensitivity of a specific retrieval estimate to its own true value. The averaging kernel matrix would be an identity matrix for the idealized scenario, i.e., each retrieval estimate is sensitive to its own true value with a 1:1 ratio but insensitive to any other state variables.

The averaging kernels of surface spectral emissivity over the mid-Arctic Ocean are shown in Figure 3. Each curve represents a row in \mathbf{A} , which usually peaks at its diagonal element. The closer the peak is to 1, the more signal from true surface emissivity on the same channel is expected to be retrieved. The averaging kernels of all mid-IR channels show essentially zero sensitivity to surface emissivity on the far-IR channels (Figure 3a and 3c). Except for the 8.4- μm channel, averaging kernels of the rest mid-IR channels all have peak values ≥ 0.5 . The 8.4- μm channel has a NeSR larger than the radiance change corresponding to the 1σ *a priori* uncertainty of the 8.4- μm surface emissivity, indicating that the *a posteriori* uncertainty cannot be further reduced from the *a priori* one by such measurements. This is why the averaging kernel for the 8.4- μm surface emissivity does not have a noticeable peak as the rest of the mid-IR channels. Moreover, averaging kernels of all mid-IR channels show little changes from January to July

despite the increase of TCWV from 0.27 to 1.31 cm (a factor of 4.9). In contrast, the averaging kernel of any far-IR surface emissivity has a positive peak smaller than 0.5 in January (Figure 3b) and remains flat at zero over all the far-IR channels in July (Figure 3d). Such contrasts in the averaging kernels between the far-IR and mid-IR channels show that the TCWV variation can affect surface emissivity retrievals in the far-IR much more than those in the mid-IR. Note that the far-IR averaging kernels in July have non-zero components over the mid-IR channels (Figure 3d), which implies that the far-IR emissivity retrievals for the mid-Arctic Ocean in July will be largely constrained by the *a priori* covariance between the far-IR and mid-IR, as well as the actual mid-IR surface emissivity retrievals in July.

The averaging kernels for the Antarctic Plateau are shown in Figure 4. The most noticeable difference from Figure 3 is that, in both January and July, the averaging kernels for the far-IR surface emissivities have a much higher peak over the respective channels. This is due to the much smaller TCWV over the Antarctic Plateau than the mid-Arctic Ocean. In this case, the far-IR surface emissivity retrievals are more influenced by the actual far-IR measurements than the *a priori* constraints between the far-IR and mid-IR.

To further quantitatively understand how the TCWV affects the information contents for the mid-IR and far-IR emissivity retrievals, we perform a DoF analysis. The DoF for signal, denoted by d_s , refers to the number of independent pieces of information about the true state that can be determined from a measurement. It tells how informative the observation can be considering the measurement noise and the *a priori* dependence among surface spectral emissivity. The DoF for signal is equal to the trace of averaging kernel matrix \mathbf{A} . Using monthly-mean January profiles over the mid-Arctic Ocean, we scale the water vapor profile to get different TCWV and compute the DoF for signal accordingly. The DoF calculation is not sensitive to the choice of months or

polar surface types. Figure 5 shows the DoFs for surface emissivity retrievals in the mid-IR and far-IR, respectively, as a function of TCWV derived in this way. Shaded areas denote the long-term monthly-mean range of TCWV for the Arctic (60-90°N, 0-360°E), Antarctic (60-90°S, 0-360°E) and globe, respectively. In general, the polar regions have less water vapor abundance than global mean by a factor of 2.5 to 10. The Arctic exhibits a larger seasonal variation of TCWV than the Antarctic. When the TCWV is around 0.005 cm, the DoF of six mid-IR channels is 4.7, and the DoF for signal of eight far-IR channels is 6.2. This discrepancy between DoFs and the corresponding number of channels reflects the influence of instrument noise and correlations among PREFIRE channels characterized by the *a priori* covariance matrix. As the TCWV increases, the DoF for the far-IR surface emissivity retrievals drops to 4 when TCWV = 0.1 cm and to virtually zero when TCWV > 1 cm. In contrast, the DoF for the mid-IR surface emissivity retrievals stays relatively constant until the TCWV reaches 1 cm. If we take 0.5 as a threshold of the DoF, the far-IR and mid-IR surface emissivity retrieval drop to this threshold when the TCWV reaches 0.6 cm and 3 cm, respectively (Figure 5). Such variations with the TCWV are consistent with what is shown in Figure 3 and Figure 4, corroborating that the retrievals of far-IR surface emissivity can be significantly influenced by the water vapor abundance while the mid-IR retrievals are less affected by the TCWV.

4.2 Performance assessment of the retrieval algorithm

The retrieval algorithm described in Section 3 is applied to 960 synthetic PREFIRE clear-sky spectra (i.e., 240 spectra from January, April, July, and October, respectively). To assess the performance of the surface emissivity retrieval algorithm, the ERA5 temperature and humidity profiles used here are assumed to be accurate without errors. The influence of uncertainty in temperature and humidity profiles on the surface emissivity retrieval will be discussed in the next

section. Figure 6 shows an individual retrieval in April over the deep Arctic. The true surface emissivity at each channel falls into the range within the *a posteriori* uncertainty (Figure 6a) of the optimal estimate. The radiances computed from the retrieved surface emissivity (red circled line in Figure 6b) are close to the synthetic PREFIRE radiances (blue dotted line in Figure 6b). The differences between them, i.e. radiance residuals, are within $\pm 0.03 \text{ Wm}^{-2}\text{sr}^{-1}\mu\text{m}^{-1}$ as shown in Figure 6c and all fall into the NeSR range ($\pm 1\sigma$) denoted by the shading.

All 960 cases converged within 15 iterations, with a median convergence speed of 8 iterations. Radiance residuals of the 960 cases show no dependence on the synthetic radiances, as one example given in Figure 7a for a far-IR channel at $16.9 \mu\text{m}$. Moreover, the overwhelming majority of radiance residuals fall within the range determined by the NeSR of this channel, indicating that the accuracy level of retrieval results is comparable to the instrument noise level (Figure 7a). The residuals also show no dependence on TCWV (Figure 7b). This good fit between retrieval estimates and synthetic observations is stable regardless of measurement noise or the variation of water vapor abundance. Thus, Figure 7a and 7b assure that the optimal estimation algorithm performs as intended.

Figure 8a summarizes the mean bias and RMSE of the retrieval results for all 960 cases. The mean bias varies within ± 0.01 for both mid-IR and far-IR channels. The RMSEs on the far-IR channels are less than 0.024 and generally larger than those in the mid-IR. When it comes to each calendar month studied here, the mean bias shows no obvious seasonal dependence, neither do the RMSEs on the mid-IR channels. However, the RMSEs on the far-IR channels are larger in July than in other months (Figure 8c). This is consistent with the aforementioned information content analysis: the far-IR retrieval in July over the Arctic relies more on the *a priori* constraints between the mid-IR and far-IR channels as well as the mid-IR retrievals than the actual far-IR

radiances. In other words, the *a priori* knowledge becomes the predominant factor determining the Arctic far-IR surface emissivity retrievals in July, which has been demonstrated by the zero (flat) averaging kernels of the far-IR channels in Figure 3d.

4.3 Sensitivity of retrievals to the *a priori* constraint

The *a priori* information exerts influence on the optimal estimation retrievals by providing an important constraint within the Bayesian framework. If the true surface emissivity spectra are not properly characterized by the *a priori* mean and covariance matrix, the retrieval results can be significantly different from the true values (Maahn et al., 2020). Some studies, such as the retrievals of liquid water path from ground-based measurements (Turner et al., 2007), may find little dependence on the *a priori* constraint when the observations are accurate enough and can always provide adequate information content. However, for the PREFIRE surface emissivity retrievals studied here, we need to further understand how the retrieval results can be influenced by the different choices of *a priori* constraint.

Two *a priori* covariance matrices are tested to further understand such influence. The *a priori* covariance matrix used in Figure 8 is denoted as “informative \mathbf{S}_a ”. The other *a priori* covariance matrix, termed as “weakly informative \mathbf{S}_a ”, is a diagonal matrix with a uniform value of 0.15^2 on its diagonal. This weakly informative \mathbf{S}_a assumes the same *a priori* uncertainty ($\sigma=0.15$) for the emissivity at every channel but no *a priori* correlation between surface emissivities at any two different channels. Figure 9 compares the mean and RMSE of the retrieval results using these distinct \mathbf{S}_a (note that the results using informative \mathbf{S}_a are the same as what is shown in Figure 8a). Using weakly informative \mathbf{S}_a instead of the informative \mathbf{S}_a leads to larger RMSEs for all channels and such differences are much more noticeable in the far-IR than in the mid-IR: the RMSEs derived using the two different \mathbf{S}_a can differ by 0.002-0.06 in the mid-IR but by 0.04-

0.12 in the far-IR. Therefore, the far-IR surface emissivity retrievals in the Arctic are more influenced by choice of \mathbf{S}_a than the mid-IR surface emissivity retrievals. Nevertheless, even for the case of weakly informative \mathbf{S}_a , the RMSEs are smaller than *a priori* uncertainty (i.e., 0.15) for all channels, with the largest RMSE being 0.14 at the 18.6- μm channel. The reduction from the *a priori* uncertainty reflects the extent to which the PREFIRE measurements with noise can help constrain the retrievals. The larger the reduction, the more the retrieval results are determined by the measurements than *a priori*. Not only the retrieval accuracy but also the convergence speed can benefit from a properly constructed *a priori* constraint. When using the weakly informative \mathbf{S}_a , 72% of the 960 cases converge within 10 iterations and 96% converge within 15 iterations. When the informative \mathbf{S}_a is used, 98% cases converge within 10 iterations and 100% converge within 15 iterations. Therefore, adopting a properly constructed \mathbf{S}_a is critical to the satisfactory performance of the retrieval algorithm, especially for the far-IR surface emissivity retrievals.

Besides above discussion, the OE retrieval framework used here assumes that *a priori* distribution of the retrieved variable follows the normal distribution. A deviation from such normal distribution could lead to an incorrect estimation of *posteriori* error covariance. The mid-IR surface spectral emissivity in Huang et al. (2016) is based on the MODIS retrieved surface emissivity retrieved at 0.05°-by-0.05° spatial resolution. The histogram of a mid-IR channel over the Arctic in a given calendar month indeed resemble a Gaussian curve. As for the surface emissivities in the far-IR channels, measurements are not available for validating its distribution. Thus, our assessment of *posteriori* error covariance here might be affected by such a possibility of non-Gaussian *a priori* distribution. We also notice that the Gaussian-like histogram is more applicable to each polar region and each calendar month, but not to both polar regions together

or the entire year. Therefore, in actual retrieval, there is a need of constructing *a priori* covariance separately for each region and each month (or minimally each season).

5. Conclusions and discussion

In preparation for the PREFIRE mission, this study seeks to implement and assess an optimal-estimation-based surface emissivity retrieval algorithm. Fourteen mid-IR and far-IR PREFIRE channels are selected for the feasibility of retrieving their surface spectral emissivities in the polar regions. The information content analysis evaluates to what extent the PREFIRE measurements can provide useful information in addition to the *a priori* constraints. Both averaging kernel and the DoF analyses demonstrate that the mid-IR information content is less affected by the TCWV than the far-IR counterpart. When the TCWV is > 1 cm, the information content available for far-IR surface emissivity retrievals dramatically decreases to virtually zero.

The optimal estimation retrieval algorithm is applied to retrieve surface spectral emissivity from 960 synthetic PREFIRE clear-sky radiance spectra spanning the range of conditions encountered at both poles with random noise added to each channel based on the current estimation of the PREFIRE NeSR. The retrievals of all 960 cases converge within 15 iterations. The mean of retrieval bias varies within ± 0.01 over both mid-IR and far-IR channels. The RMSEs in the mid-IR range from 0.005 to 0.02, while those in the far-IR stay around 0.02. The RMSEs of far-IR surface emissivity retrievals in the Arctic, unlike those in the mid-IR, exhibit a noticeable seasonal dependence, with the largest RMSEs seen in July among four calendar months examined in this study. The comparison of retrieval results using two different *a priori* covariance matrices indicates that the mid-IR surface emissivity retrievals are much less affected by the choice of *a priori* covariance than the far-IR surface emissivity retrievals do. For the same

retrieval algorithm, the choice of *a priori* covariance can affect the convergence speed as well as the retrieval accuracy level.

This study assumes the temperature and humidity profiles as well as surface skin temperature are known without any uncertainty. This assumption is necessary given the spectral resolution of the PREFIRE channels (i.e., 0.84 μm). MODIS infrared channels have a narrower spectral resolution (i.e., $\sim 0.3\text{-}0.5$ μm) than the PREFIRE, and its surface emissivity retrieval algorithm also assumed that the temperature and humidity profiles were known from either the numerical weather forecast data assimilation or collocated other remote sensing observations (Hulley et al., 2016). However, such temperature and humidity profiles always have uncertainties. In a real operational algorithm, how such uncertainties can propagate and affect the surface emissivity retrievals needs to be understood and quantified. As demonstrated by several validation studies of the atmospheric temperature and humidity retrievals (Divakarla et al., 2006; Pougatchev et al., 2009; Divakarla et al., 2014; Boylan et al., 2015; Milstein & Blackwell, 2016; Nalli et al., 2018), atmospheric temperature profiles from data assimilation or reanalysis are generally in good agreement with those inverted from hyperspectral soundings or directly observed by radiosondes, and the RMSEs are around or less than 1.5 K in the troposphere. In contrast, state-of-the-art humidity retrievals from hyperspectral sounders still can have a RMSE as large as 20% in the troposphere (Milstein & Blackwell, 2016; Nalli et al., 2018), and reanalysis humidity fields bear similar uncertainty (Jakobson et al., 2012; Nygård et al., 2016; Chen et al., 2018). Therefore, the uncertainties in the humidity profiles likely can affect the surface emissivity retrievals more than those in the temperature profiles. Quantifying the error propagation of such uncertainties in the humidity and temperature profiles is out of the scope of this study but will be investigated once the data flow structure for the entire PREFIRE operational algorithm is determined.

This study highlights, in multiple ways, the importance of *a priori* covariance on the surface spectral emissivity retrieval. Therefore, having *a priori* covariance with correct and sufficient representation of polar surface spectral emissivity, and testing its deviation from assumed Gaussian distribution, are crucial to the success of the PREFIRE surface spectral emissivity retrieval effort. Likewise, future work upon knowing the instrumental characteristics of PREFIRE after the launch can be conducted to consider the impact of the off-diagonal observation error covariance matrix on the surface emissivity retrieval. While there have been a couple of field campaigns to measure the far-IR surface spectral emissivities over Greenland and Mt. Zugspitze in the German Alps (Bellisario et al., 2017; Murray et al., 2020; Palchetti et al., 2021), we hope that our findings here can further motivate more in-situ or laboratory measurements of such quantities, especially over the far-IR dirty window where few actual measurements currently exist.

Acknowledgments

We wish to thank three anonymous reviewers for their thoughtful comments. We are thankful to X. Liu at NASA Langley for making the PCRTM code available to us. This research was carried out at the University of Michigan, Ann Arbor, and supported by the NASA PREFIRE mission under grant 80NSSC18K1485 with a subcontract from the University of Wisconsin. Portions of this research were carried out at the Jet Propulsion Laboratory, California Institute of Technology, under contract with the National Aeronautics and Space Administration. The ERA5 data were obtained from <https://cds.climate.copernicus.eu/>. The global surface spectral emissivity data can be obtained from <https://huang.engin.umich.edu/182-2/>.

References

- Backus, G., Gilbert, F., & Bullard, E. C. (1970). Uniqueness in the inversion of inaccurate gross Earth data. *Philosophical Transactions of the Royal Society of London. Series A, Mathematical and Physical Sciences*, 266(1173), 123-192. doi:10.1098/rsta.1970.0005
- Bantges, R. J., Brindley, H. E., Chen, X. H., Huang, X. L., Harries, J. E., & Murray, J. E. (2016). On the Detection of Robust Multidecadal Changes in Earth's Outgoing Longwave Radiation Spectrum. *Journal of Climate*, 29(13), 4939-4947. doi:10.1175/jcli-d-15-0713.1
- Becker, F., & Li, Z.-L. (1990a). Temperature-independent spectral indices in thermal infrared bands. *Remote Sensing of Environment*, 32(1), 17-33. doi:10.1016/0034-4257(90)90095-4
- Becker, F., & Li, Z.-L. (1990b). Towards a local split window method over land surfaces. *International Journal of Remote Sensing*, 11(3), 369-393. doi:10.1080/01431169008955028
- Bellisario, C., Brindley, H. E., Murray, J. E., Last, A., Pickering, J., Harlow, R. C., et al. (2017). Retrievals of the Far Infrared Surface Emissivity Over the Greenland Plateau Using the Tropospheric Airborne Fourier Transform Spectrometer (TAFTS). *Journal of Geophysical Research: Atmospheres*, 122(22), 112,152-112,166. doi:10.1002/2017JD027328

- Berk, A., Anderson, G. P., Acharya, P. K., Bernstein, L. S., Muratov, L., Lee, J., et al. (2006). MODTRAN5: 2006 update. Paper presented at the Proc.SPIE 6233, Algorithms and Technologies for Multispectral, Hyperspectral, and Ultraspectral Imagery XII. doi:10.1117/12.665077
- Boylan, P., Wang, J., Cohn, S. A., Fetzer, E., Maddy, E. S., & Wong, S. (2015). Validation of AIRS version 6 temperature profiles and surface-based inversions over Antarctica using Concordiasi dropsonde data. *Journal of Geophysical Research: Atmospheres*, 120(3), 992-1007. doi:10.1002/2014JD022551
- Canas, T., Murray, J., & Harries, J. (1997). Tropospheric airborne Fourier transform spectrometer (TAFTS). *Proc. SPIE, Satellite Remote Sensing of Clouds and the Atmosphere II*, 3220. doi:10.1117/12.301139
- Capelle, V., Chédin, A., Péquignot, E., Schlüssel, P., Newman, S. M., & Scott, N. A. (2012). Infrared Continental Surface Emissivity Spectra and Skin Temperature Retrieved from IASI Observations over the Tropics. *Journal of Applied Meteorology and Climatology*, 51(6), 1164-1179. doi:10.1175/JAMC-D-11-0145.1
- Carissimo, A., De Feis, I., & Serio, C. (2005). The physical retrieval methodology for IASI: the δ -IASI code. *Environmental Modelling & Software*, 20(9), 1111-1126. doi:10.1016/j.envsoft.2004.07.003
- Chen, X., Huang, X., Dong, X., Xi, B., Dolinar, E. K., Loeb, N. G., et al. (2018). Using AIRS and ARM SGP Clear-Sky Observations to Evaluate Meteorological Reanalyses: A Hyperspectral Radiance Closure Approach. *Journal of Geophysical Research: Atmospheres*, 123(20), 11,720-711,734. doi:10.1029/2018JD028850
- Chen, X., Huang, X., & Flanner, M. G. (2014). Sensitivity of modeled far-IR radiation budgets in polar continents to treatments of snow surface and ice cloud radiative properties. *Geophysical Research Letters*, 41(18), 6530-6537. doi:10.1002/2014GL061216
- Chen, X., Huang, X., & Liu, X. (2013). Non-negligible effects of cloud vertical overlapping assumptions on longwave spectral fingerprinting studies. *Journal of Geophysical Research: Atmospheres*, 118(13), 7309-7320. doi:10.1002/jgrd.50562
- Christensen, P. R., Bandfield, J. L., Hamilton, V. E., Ruff, S. W., Kieffer, H. H., Titus, T. N., et al. (2001). Mars Global Surveyor Thermal Emission Spectrometer experiment: Investigation description and surface science results. *Journal of Geophysical Research: Planets*, 106(E10), 23823-23871. doi:10.1029/2000JE001370
- Clough, S. A., Shephard, M. W., Mlawer, E. J., Delamere, J. S., Iacono, M. J., Cady-Pereira, K., et al. (2005). Atmospheric radiative transfer modeling: a summary of the AER codes. *Journal of Quantitative Spectroscopy and Radiative Transfer*, 91(2), 233-244. doi:10.1016/j.jqsrt.2004.05.058

- Coll, C., Caselles, V., Valor, E., & Rubio, E. (2003). Validation of temperature-emissivity separation and split-window methods from TIMS data and ground measurements. *Remote Sensing of Environment*, 85(2), 232-242. doi:10.1016/S0034-4257(03)00003-8
- Dee, D. P., Uppala, S. M., Simmons, A. J., Berrisford, P., Poli, P., Kobayashi, S., et al. (2011). The ERA-Interim reanalysis: configuration and performance of the data assimilation system. *Quarterly Journal of the Royal Meteorological Society*, 137(656), 553-597. doi:10.1002/qj.828
- Divakarla, M., Barnet, C., Liu, X., Gu, D., Wilson, M., Kizer, S., et al. (2014). The CrIMSS EDR Algorithm: Characterization, Optimization, and Validation. *Journal of Geophysical Research: Atmospheres*, 119(8), 4953-4977. doi:10.1002/2013JD020438
- Divakarla, M. G., Barnet, C. D., Goldberg, M. D., McMillin, L. M., Maddy, E., Wolf, W., et al. (2006). Validation of Atmospheric Infrared Sounder temperature and water vapor retrievals with matched radiosonde measurements and forecasts. *Journal of Geophysical Research: Atmospheres*, 111(D9). doi:10.1029/2005JD006116
- Feldman, D. R., Collins, W. D., Pincus, R., Huang, X., & Chen, X. (2014). Far-infrared surface emissivity and climate. *Proceedings of the National Academy of Sciences*, 111(46), 16297. doi:10.1073/pnas.1413640111
- Fisher, J. B., Lee, B., Purdy, A. J., Halverson, G. H., Dohlen, M. B., Cawse-Nicholson, K., et al. (2020). ECOSTRESS: NASA's Next Generation Mission to Measure Evapotranspiration From the International Space Station. *Water Resources Research*, 56(4), e2019WR026058. doi:10.1029/2019WR026058
- Fisher, R. A. (1922). On the mathematical foundations of theoretical statistics. *Philosophical Transactions of the Royal Society of London. Series A, Containing Papers of a Mathematical or Physical Character*, 222(594-604), 309-368. doi:10.1098/rsta.1922.0009
- French, A. N., Schmugge, T. J., Ritchie, J. C., Hsu, A., Jacob, F., & Ogawa, K. (2008). Detecting land cover change at the Jornada Experimental Range, New Mexico with ASTER emissivities. *Remote Sensing of Environment*, 112(4), 1730-1748. doi:10.1016/j.rse.2007.08.020
- Gillespie, A. (1986). *Lithologic mapping of silicate rocks using TIMS*. Jet Propulsion Lab., California Inst. of Tech. Pasadena, CA: The TIMS Data User's Workshop Retrieved from <https://ntrs.nasa.gov/citations/19870007685>

Gillespie, A., Rokugawa, S., Matsunaga, T., Cothern, J. S., Hook, S., & Kahle, A. B. (1998). A temperature and emissivity separation algorithm for Advanced Spaceborne Thermal Emission and Reflection Radiometer (ASTER) images. *IEEE Transactions on Geoscience and Remote Sensing*, *36*(4), 1113-1126.

doi:10.1109/36.700995

Hanel, R. A., Schlachman, B., Rogers, D., & Vanous, D. (1971). Nimbus 4 Michelson Interferometer. *Applied Optics*, *10*(6), 1376-1382. doi:10.1364/AO.10.001376

Hersbach, H., Bell, B., Berrisford, P., Hirahara, S., Horányi, A., Muñoz-Sabater, J., et al. (2020). The ERA5 global reanalysis. *Quarterly Journal of the Royal Meteorological Society*, *146*(730), 1999-2049.

doi:10.1002/qj.3803

Huang, X., Chen, X., Flanner, M., Yang, P., Feldman, D., & Kuo, C. (2018). Improved Representation of Surface Spectral Emissivity in a Global Climate Model and Its Impact on Simulated Climate. *Journal of Climate*, *31*(9), 3711-3727. doi:10.1175/jcli-d-17-0125.1

Huang, X., Chen, X., Soden, B. J., & Liu, X. (2014). The spectral dimension of longwave feedback in the CMIP3 and CMIP5 experiments. *Geophysical Research Letters*, *41*(22), 7830-7837. doi:10.1002/2014GL061938

Huang, X., Chen, X., Zhou, D. K., & Liu, X. (2016). An Observationally Based Global Band-by-Band Surface Emissivity Dataset for Climate and Weather Simulations. *Journal of the Atmospheric Sciences*, *73*(9), 3541-3555. doi:10.1175/jas-d-15-0355.1

Hulley, G., Malakar, N., & Freepartner, R. (2016). *Moderate Resolution Imaging Spectroradiometer (MODIS) Land Surface Temperature and Emissivity Product (MxD21) Algorithm Theoretical Basis Document Collection-6*. JPL Publication Retrieved from https://lpdaac.usgs.gov/documents/107/MOD21_ATBD.pdf

Hulley, G. C., Hook, S. J., Abbott, E., Malakar, N., Islam, T., & Abrams, M. (2015). The ASTER Global Emissivity Dataset (ASTER GED): Mapping Earth's emissivity at 100 meter spatial scale. *Geophysical Research Letters*, *42*(19), 7966-7976. doi:10.1002/2015GL065564

Hulley, G. C., Malakar, N. K., Islam, T., & Freepartner, R. J. (2018). NASA's MODIS and VIIRS Land Surface Temperature and Emissivity Products: A Long-Term and Consistent Earth System Data Record. *IEEE Journal of Selected Topics in Applied Earth Observations and Remote Sensing*, *11*(2), 522-535.

doi:10.1109/JSTARS.2017.2779330

Jakobson, E., Vihma, T., Palo, T., Jakobson, L., Keernik, H., & Jaagus, J. (2012). Validation of atmospheric reanalyses over the central Arctic Ocean. *Geophysical Research Letters*, 39(10). doi:10.1029/2012GL051591

Kidder, S. Q., KIDDER, R. M., & Vonder Haar, T. H. (1995). *Satellite Meteorology: An Introduction* (1st ed. 466 pp): Academic Press, ISBN: 9780124064300.

L'Ecuyer, T. S., Drouin, B. J., Anheuser, J., Grames, M., Henderson, D., Huang, X., et al. (2021). The Polar Radiant Energy in the Far InfraRed Experiment: A New Perspective on Polar Longwave Energy Exchanges. *Bulletin of the American Meteorological Society*, 1-46. doi:10.1175/BAMS-D-20-0155.1

L'Ecuyer, T. S., & Stephens, G. L. (2002). An Estimation-Based Precipitation Retrieval Algorithm for Attenuating Radars. *Journal of Applied Meteorology*, 41(3), 272-285. doi:10.1175/1520-0450(2002)041<0272:AEBPRA>2.0.CO;2

Li, J., Li, J., Weisz, E., & Zhou, D. K. (2007). Physical retrieval of surface emissivity spectrum from hyperspectral infrared radiances. *Geophysical Research Letters*, 34(16). doi:10.1029/2007GL030543

Li, Z.-L., Wu, H., Wang, N., Qiu, S., Sobrino, J. A., Wan, Z., et al. (2013). Land surface emissivity retrieval from satellite data. *International Journal of Remote Sensing*, 34(9-10), 3084-3127. doi:10.1080/01431161.2012.716540

Liu, X., Smith, W. L., Zhou, D. K., & Larar, A. (2006). Principal component-based radiative transfer model for hyperspectral sensors: theoretical concept. *Applied Optics*, 45(1), 201-209. doi:10.1364/AO.45.000201

Liu, X., Zhou, D. K., Larar, A. M., Smith, W. L., Schluessel, P., Newman, S. M., et al. (2009). Retrieval of atmospheric profiles and cloud properties from IASI spectra using super-channels. *Atmos. Chem. Phys.*, 9(23), 9121-9142. doi:10.5194/acp-9-9121-2009

Maahn, M., Turner, D. D., Löhnert, U., Posselt, D. J., Ebell, K., Mace, G. G., & Comstock, J. M. (2020). Optimal Estimation Retrievals and Their Uncertainties: What Every Atmospheric Scientist Should Know. *Bulletin of the American Meteorological Society*, 101(9), E1512-E1523. doi:10.1175/bams-d-19-0027.1

Masiello, G., Serio, C., & Antonelli, P. (2012). Inversion for atmospheric thermodynamical parameters of IASI data in the principal components space. *Quarterly Journal of the Royal Meteorological Society*, 138(662), 103-117. doi:10.1002/qj.909

Milstein, A. B., & Blackwell, W. J. (2016). Neural network temperature and moisture retrieval algorithm validation for AIRS/AMSU and CrIS/ATMS. *Journal of Geophysical Research: Atmospheres*, *121*(4), 1414-1430. doi:10.1002/2015JD024008

Murray, J. E., Brindley, H. E., Fox, S., Bellisario, C., Pickering, J. C., Fox, C., et al. (2020). Retrievals of High-Latitude Surface Emissivity Across the Infrared From High-Altitude Aircraft Flights. *Journal of Geophysical Research: Atmospheres*, *125*(22), e2020JD033672. doi:10.1029/2020JD033672

Nalli, N. R., Gambacorta, A., Liu, Q., Barnet, C. D., Tan, C., Iturbide-Sanchez, F., et al. (2018). Validation of Atmospheric Profile Retrievals From the SNPP NOAA-Unique Combined Atmospheric Processing System. Part 1: Temperature and Moisture. *IEEE Transactions on Geoscience and Remote Sensing*, *56*(1), 180-190. doi:10.1109/TGRS.2017.2744558

Nygård, T., Vihma, T., Birnbaum, G., Hartmann, J., King, J., Lachlan-Cope, T., et al. (2016). Validation of eight atmospheric reanalyses in the Antarctic Peninsula region. *Quarterly Journal of the Royal Meteorological Society*, *142*(695), 684-692. doi:10.1002/qj.2691

Palchetti, L., Brindley, H., Bantges, R., Buehler, S. A., Camy-Peyret, C., Carli, B., et al. (2020). FORUM: Unique Far-Infrared Satellite Observations to Better Understand How Earth Radiates Energy to Space. *Bulletin of the American Meteorological Society*, *101*(12), E2030-E2046. doi:10.1175/bams-d-19-0322.1

Palchetti, L., Barucci, M., Belotti, C., Bianchini, G., Cluzet, B., D'Amato, F., Del Bianco, S., Di Natale, G., Gai, M., Khordakova, D., Montori, A., Oetjen, H., Rettinger, M., Rolf, C., Schuettemeyer, D., Sussmann, R., Viciani, S., Vogelmann, H., & Wienhold, F. G. (2021). Observations of the downwelling far-infrared atmospheric emission at the Zugspitze observatory. *Earth Syst. Sci. Data*, *13*(9), 4303-4312. doi:10.5194/essd-13-4303-2021

Pan, F., Huang, X., Leroy, S. S., Lin, P., Strow, L. L., Ming, Y., & Ramaswamy, V. (2017). The Stratospheric Changes Inferred from 10 Years of AIRS and AMSU-A Radiances. *Journal of Climate*, *30*(15), 6005-6016. doi:10.1175/jcli-d-17-0037.1

Peterson, D., & Wang, J. (2013). A sub-pixel-based calculation of fire radiative power from MODIS observations: 2. Sensitivity analysis and potential fire weather application. *Remote Sensing of Environment*, *129*, 231-249. doi:10.1016/j.rse.2012.10.020

- Pougatchev, N., August, T., Calbet, X., Hultberg, T., Oduleye, O., Schlüssel, P., et al. (2009). IASI temperature and water vapor retrievals – error assessment and validation. *Atmos. Chem. Phys.*, 9(17), 6453-6458. doi:10.5194/acp-9-6453-2009
- Price, J. C. (1984). Land surface temperature measurements from the split window channels of the NOAA 7 Advanced Very High Resolution Radiometer. *Journal of Geophysical Research: Atmospheres*, 89(D5), 7231-7237. doi:10.1029/JD089iD05p07231
- Rathke, C., Fischer, J., Neshyba, S., & Shupe, M. (2002). Improving IR cloud phase determination with 20 microns spectral observations. *Geophysical Research Letters*, 29(8), 50-51-50-54. doi:10.1029/2001GL014594
- Rockwell, B. W., & Hofstra, A. H. (2008). Identification of quartz and carbonate minerals across northern Nevada using ASTER thermal infrared emissivity data—Implications for geologic mapping and mineral resource investigations in well-studied and frontier areas. *Geosphere*, 4(1), 218-246. doi:10.1130/ges00126.1
- Rodgers, C. D. (1976). Retrieval of atmospheric temperature and composition from remote measurements of thermal radiation. *Reviews of Geophysics*, 14(4), 609-624. doi:10.1029/RG014i004p00609
- Rodgers, C. D. (2000). *Inverse Methods for Atmospheric Sounding: Theory and Practice* (Vol. 2 256 pp): WORLD SCIENTIFIC, ISBN: 978-981-02-2740-1.
- Scarlat, R. C., Heygster, G., & Pedersen, L. T. (2017). Experiences With an Optimal Estimation Algorithm for Surface and Atmospheric Parameter Retrieval From Passive Microwave Data in the Arctic. *IEEE Journal of Selected Topics in Applied Earth Observations and Remote Sensing*, 10(9), 3934-3947. doi:10.1109/JSTARS.2017.2739858
- Schlüssel, P., Hultberg, T. H., Phillips, P. L., August, T., & Calbet, X. (2005). The operational IASI Level 2 processor. *Advances in Space Research*, 36(5), 982-988. doi:10.1016/j.asr.2005.03.008
- Seemann, S. W., Borbas, E. E., Knuteson, R. O., Stephenson, G. R., & Huang, H.-L. (2008). Development of a Global Infrared Land Surface Emissivity Database for Application to Clear Sky Sounding Retrievals from Multispectral Satellite Radiance Measurements. *Journal of Applied Meteorology and Climatology*, 47(1), 108-123. doi:10.1175/2007jamc1590.1
- Shannon, C. E., & Weaver, W. (1949). *The mathematical theory of communication* (144 pp). Champaign, IL, US: University of Illinois Press, ISBN: 0252725484.

- Smith, N., & Barnett, C. D. (2019). Uncertainty Characterization and Propagation in the Community Long-Term Infrared Microwave Combined Atmospheric Product System (CLIMCAPS). *Remote Sensing*, 11(10), 1227. doi:10.3390/rs11101227
- Susskind, J., Barnett, C. D., & Blaisdell, J. M. (2003). Retrieval of atmospheric and surface parameters from AIRS/AMSU/HSB data in the presence of clouds. *IEEE Transactions on Geoscience and Remote Sensing*, 41(2), 390-409. doi:10.1109/TGRS.2002.808236
- Turner, D. D., Clough, S. A., Liljegren, J. C., Clothiaux, E. E., Cady-Pereira, K. E., & Gaustad, K. L. (2007). Retrieving Liquid Water Path and Precipitable Water Vapor From the Atmospheric Radiation Measurement (ARM) Microwave Radiometers. *IEEE Transactions on Geoscience and Remote Sensing*, 45(11), 3680-3690. doi:10.1109/TGRS.2007.903703
- Turner, D. D., & Löhnert, U. (2014). Information Content and Uncertainties in Thermodynamic Profiles and Liquid Cloud Properties Retrieved from the Ground-Based Atmospheric Emitted Radiance Interferometer (AERI). *Journal of Applied Meteorology and Climatology*, 53(3), 752-771. doi:10.1175/jamc-d-13-0126.1
- Wan, Z., & Li, Z.-L. (1997). A physics-based algorithm for retrieving land-surface emissivity and temperature from EOS/MODIS data. *IEEE Transactions on Geoscience and Remote Sensing*, 35(4), 980-996. doi:10.1109/36.602541
- Wood, N. B., & L'Ecuyer, T. S. (2021). What millimeter-wavelength radar reflectivity reveals about snowfall: an information-centric analysis. *Atmos. Meas. Tech.*, 14(2), 869-888. doi:10.5194/amt-14-869-2021.
- Xu, X., J. Wang, J. Zeng, W. Hou, K. G Meyer, S. E Platnick, E. Wilcox (2018), A pilot study of shortwave spectral fingerprints of smoke aerosols above liquid clouds, *Journal of Quantitative Spectroscopy and Radiative Transfer*, 221, 38-50. doi: 10.1016/j.jqsrt.2018.09.024
- Zhou, D. K., Larar, A. M., Liu, X., Smith, W. L., Strow, L. L., Yang, P., et al. (2011). Global Land Surface Emissivity Retrieved From Satellite Ultraspectral IR Measurements. *IEEE Transactions on Geoscience and Remote Sensing*, 49(4), 1277-1290. doi:10.1109/TGRS.2010.2051036
- Zhou, D. K., Smith, W. L., Liu, X., Larar, A. M., Mango, S. A., & Huang, H.-L. (2007). Physically Retrieving Cloud and Thermodynamic Parameters from Ultraspectral IR Measurements. *Journal of the Atmospheric Sciences*, 64(3), 969-982. doi:10.1175/jas3877.1

Table 1. Basic information about the 14 PREFIRE channels selected for surface spectral emissivity retrieval in this study. In total six in the mid-IR and eight in the far-IR are selected.

Note the PREFIRE spectral resolution for each channel is around 0.84 μm .

	PREFIRE Channel No.	Central wavelength (μm)	Spectral coverage	
			Wavelength (μm)	Wavenumber (cm^{-1})
Mid-IR	10	8.44	[8.02, 8.86]	[1247, 1129]
	12	10.13	[9.70, 10.55]	[1031, 948]
	13	10.97	[10.55, 11.39]	[948, 878]
	14	11.82	[11.39, 12.24]	[878, 817]
	15	12.66	[12.24, 13.08]	[817, 765]
	16	13.50	[13.08, 13.92]	[765, 718]
Far-IR	20	16.88	[16.45, 17.30]	[608, 578]
	21	17.72	[17.30, 18.14]	[578, 551]
	22	18.57	[18.14, 18.99]	[551, 527]
	23	19.41	[18.99, 19.83]	[527, 504]
	24	20.25	[19.83, 20.67]	[504, 484]
	25	21.10	[20.67, 21.52]	[484, 465]
	26	21.94	[21.52, 22.36]	[465, 447]
	27	22.78	[22.36, 23.20]	[447, 431]

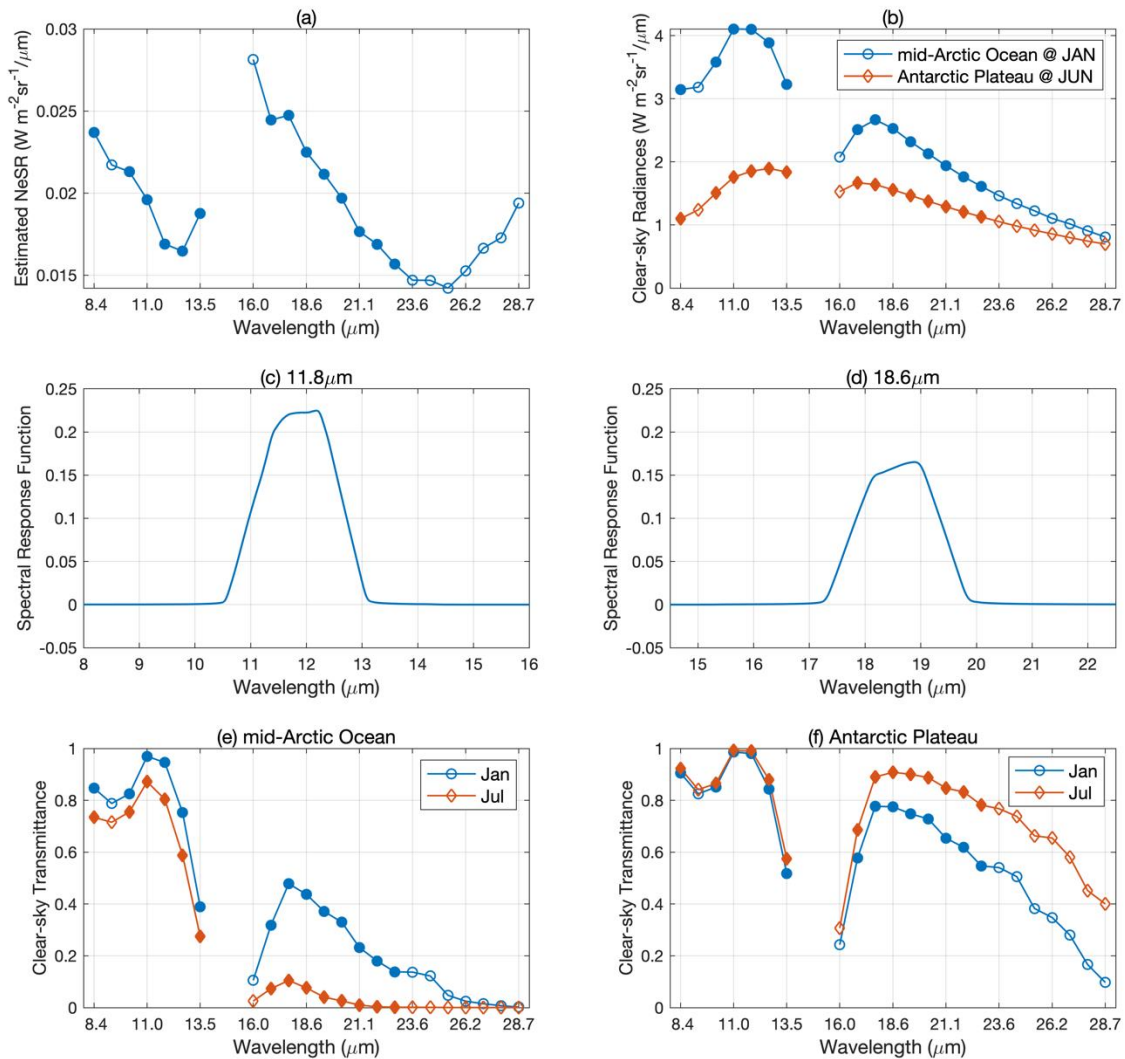


Figure 1. (a) The noise equivalent spectral radiances (NeSRs) of the PREFIRE channels in the mid-IR window region and a portion of the far-IR. (b) Simulated PREFIRE clear-sky radiances at TOA over the same channels as shown in (a). Blue and red curves represent monthly mean synthetic PREFIRE radiances over the mid-Arctic Ocean (73-77°N, 0-360°E) in January 2005 and the Antarctic Plateau (75-85°S, 60-90°E) in July 2005, respectively. Details of the simulation are described in Section 2. (c) PREFIRE spectral response function of a mid-IR channel centered on 11.8 μm . (d) Same as (c) but for a far-IR channel centered on 18.6 μm . (e) Clear-sky atmospheric transmittance averaged over the mid-Arctic Ocean at each PREFIRE channel. Blue

line with circles is for January and red line with diamonds is for July, respectively. The transmittance is computed using MODTRAN5 (MODerate resolution atmospheric TRANsmission; Berk et al., 2006). (f) Same as (e) but for the Antarctic Plateau. In all panels, solid markers denote 14 selected channels for the surface emissivity retrieval.

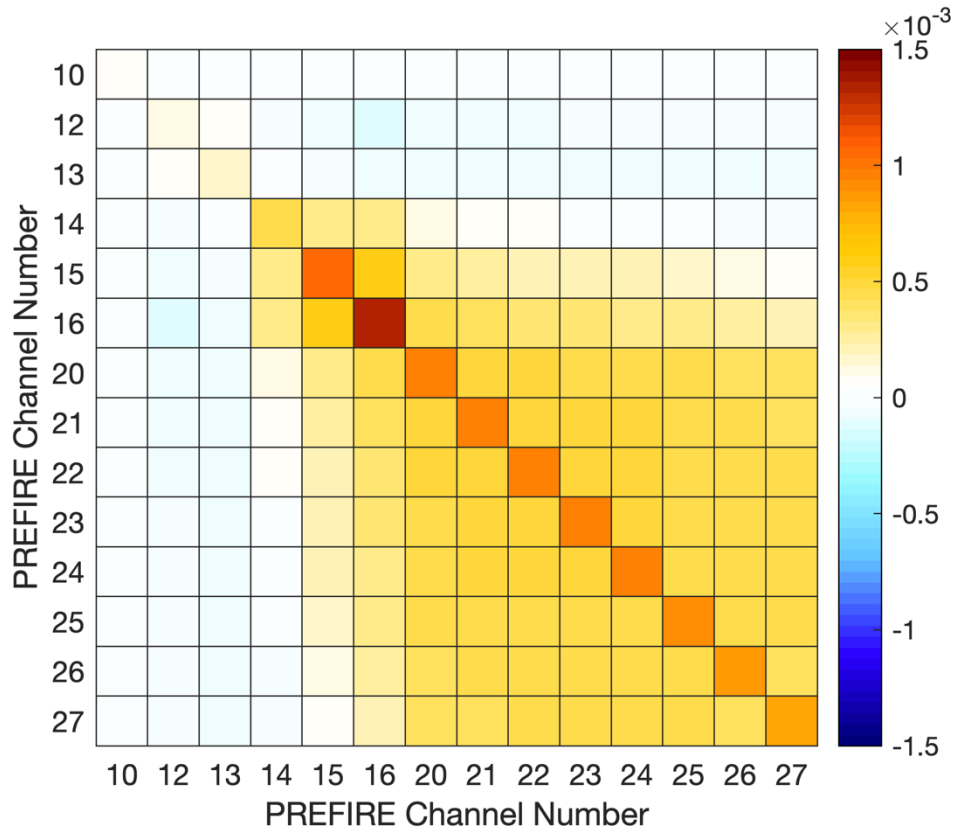


Figure 2. *A priori* covariance matrix, \mathbf{S}_a , used in our surface emissivity retrievals. The PREFIRE channel information can be found in Table 1. Details about how \mathbf{S}_a is constructed can be found in Section 3.2.

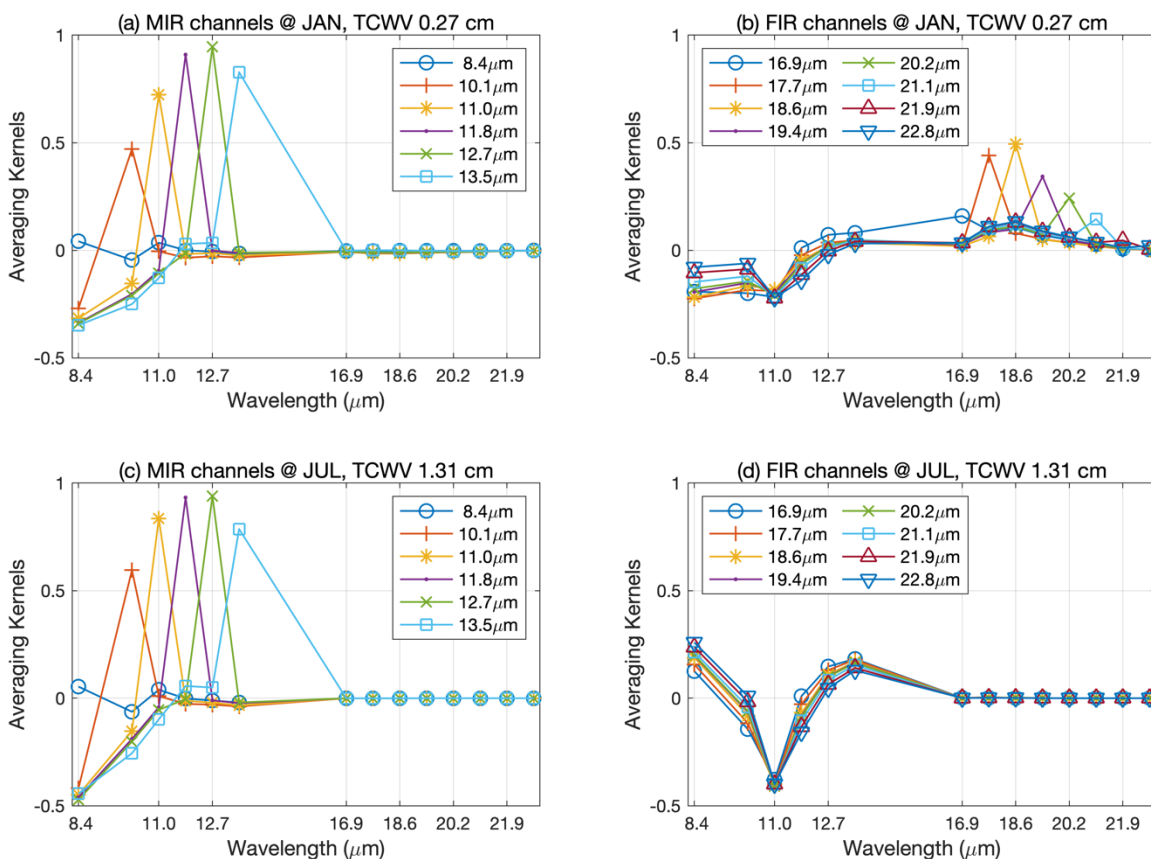


Figure 3. (a) The averaging kernels of surface spectral emissivities at the selected PREFIRE mid-IR channels. They are calculated using the ERA5 20-year (2001-2020) mean profile in January over the mid-Arctic Ocean ($73\text{-}77^{\circ}\text{N}$, $0\text{-}360^{\circ}\text{E}$). The corresponding mean total column water vapor (TCWV) is labeled on the top of the panel. (b) Same as (a) except for the averaging kernels of surface spectral emissivities at the selected far-IR channels. (c)-(d) Same as (a)-(b) except for July.

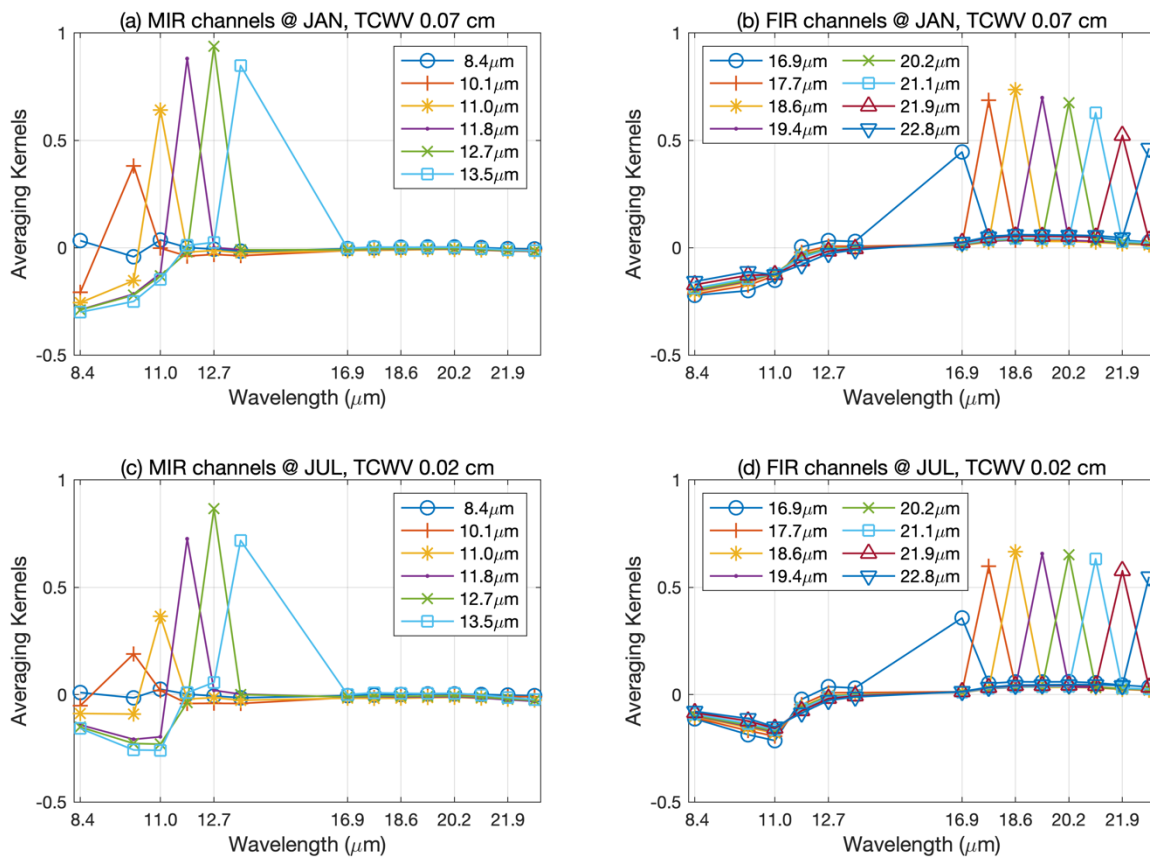


Figure 4. Same as Figure 3, but for the Antarctic Plateau (75-85°S, 60-90°E).

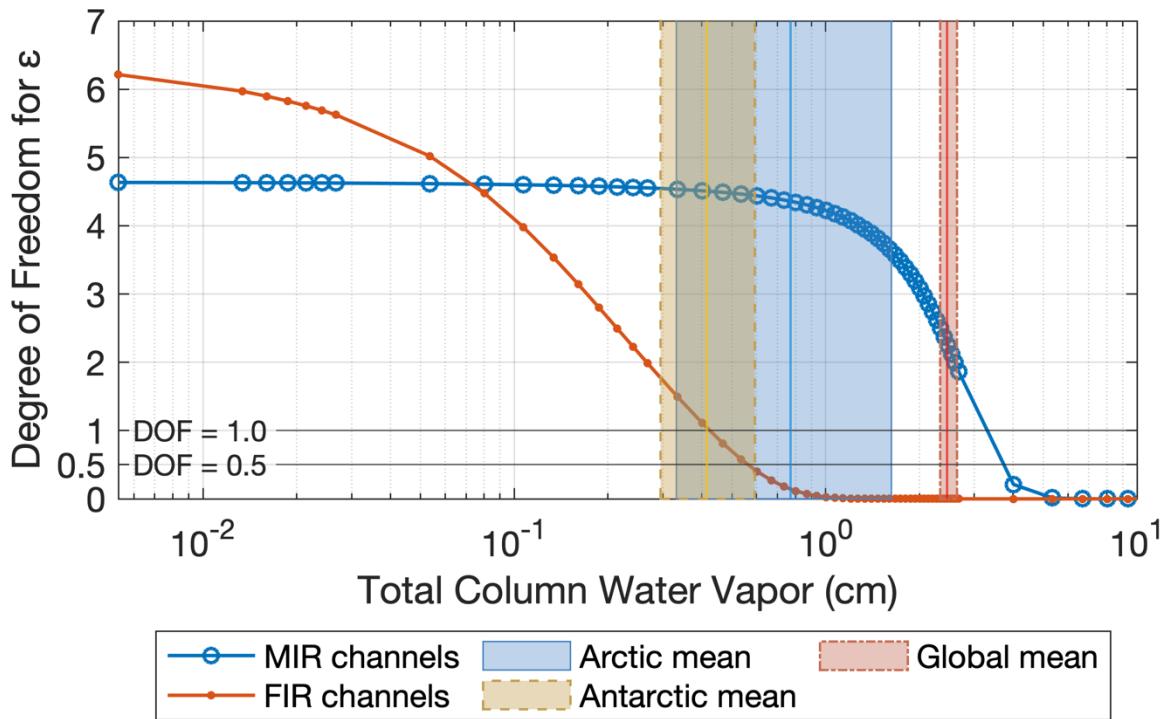


Figure 5. Degree of freedom (DoF) for the surface spectral emissivity retrieval as a function of total column water vapor (TCWV). These DoFs are calculated by scaling the water vapor profile while keeping ERA5 January long-term (2001-2020) mean temperature profiles over the mid-Arctic Ocean ($73\text{-}77^{\circ}\text{N}$, $0\text{-}360^{\circ}\text{E}$) unchanged. The blue shade bounded by solid lines denote the range of long-term monthly-mean TCWV averaged over the Arctic ($60\text{-}90^{\circ}\text{N}$, $0\text{-}360^{\circ}\text{E}$) based on the ERA5 reanalysis from 2001 to 2020. Similarly, the light-yellow shade bounded by dash lines is for the Antarctic ($60\text{-}90^{\circ}\text{S}$, $0\text{-}360^{\circ}\text{E}$), and the light red shade bounded by dotted-dash lines is for the global mean. The solid lines in each shade represent the long-term (2001-2020) annual-mean TCWV over the corresponding areas.

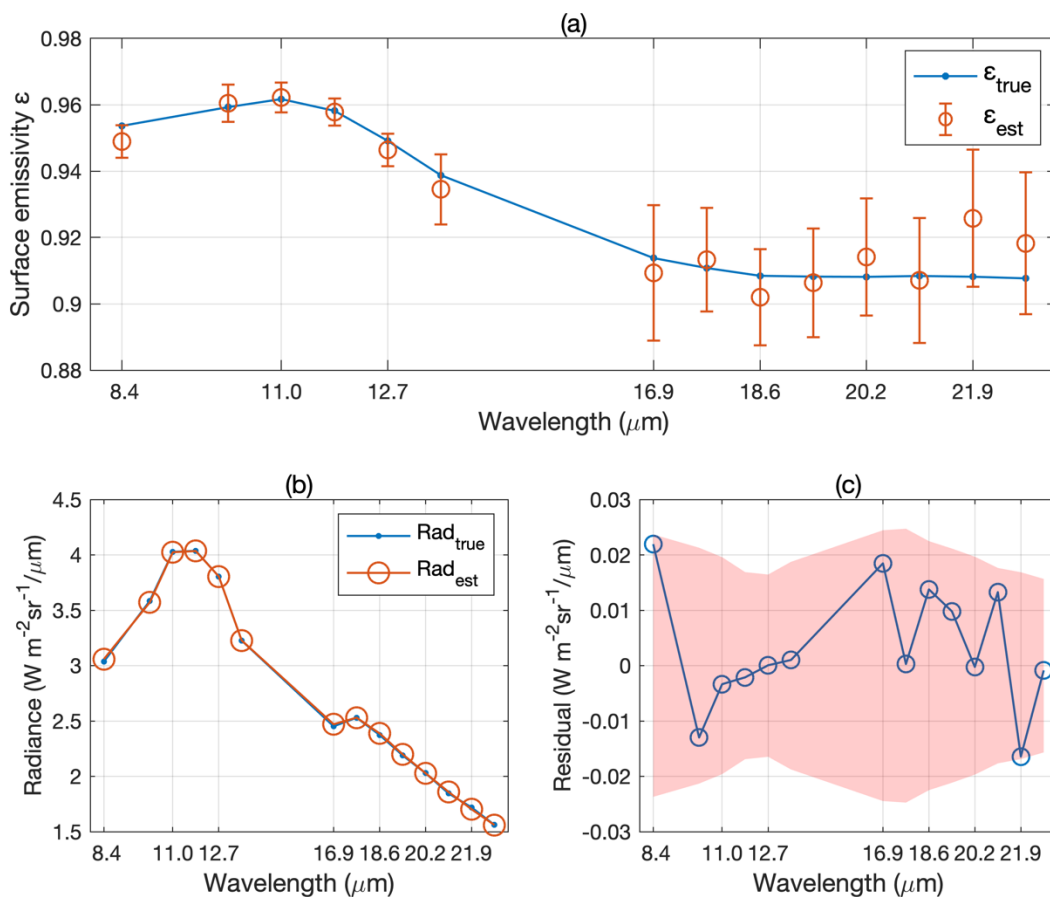


Figure 6. Retrieval of an individual April case in the Arctic. The location is 83.25°N and 343.50°E. (a) True (in blue) and retrieved (in red) surface spectral emissivity on the selected PREFIRE channels. For the retrieval estimates, open circle represents the optimal estimate of surface emissivity, and the vertical bars denote the standard deviation of retrieval uncertainty ($\pm 1\sigma$). (b) Synthetic PREFIRE radiances (in blue) and the radiances based on the retrieved surface spectral emissivity (in red). (c) Difference between the radiances shown in (b), i.e., residual radiance. Pink shade denotes the PREFIRE NeSR ($\pm 1\sigma$).

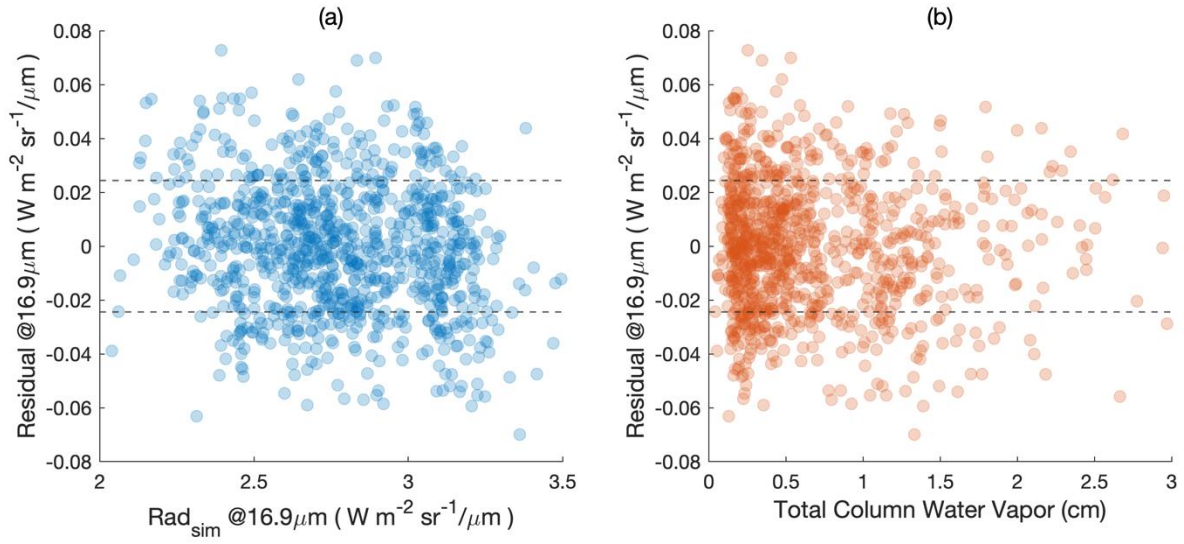


Figure 7. (a) A scatter plot of retrieval residuals with respect to the synthetic PREFIRE radiances at a far-IR channel (16.9 μm). Horizontal dash lines denote the NeSR ($\pm 1\sigma$) of this PREFIRE channel. (b) Similar to (a), but for a scatter plot of retrieval residuals at the same channel with respect to the total column water vapor. It is apparent that residuals are not correlated with the synthetic radiance, nor with the total column water vapor.

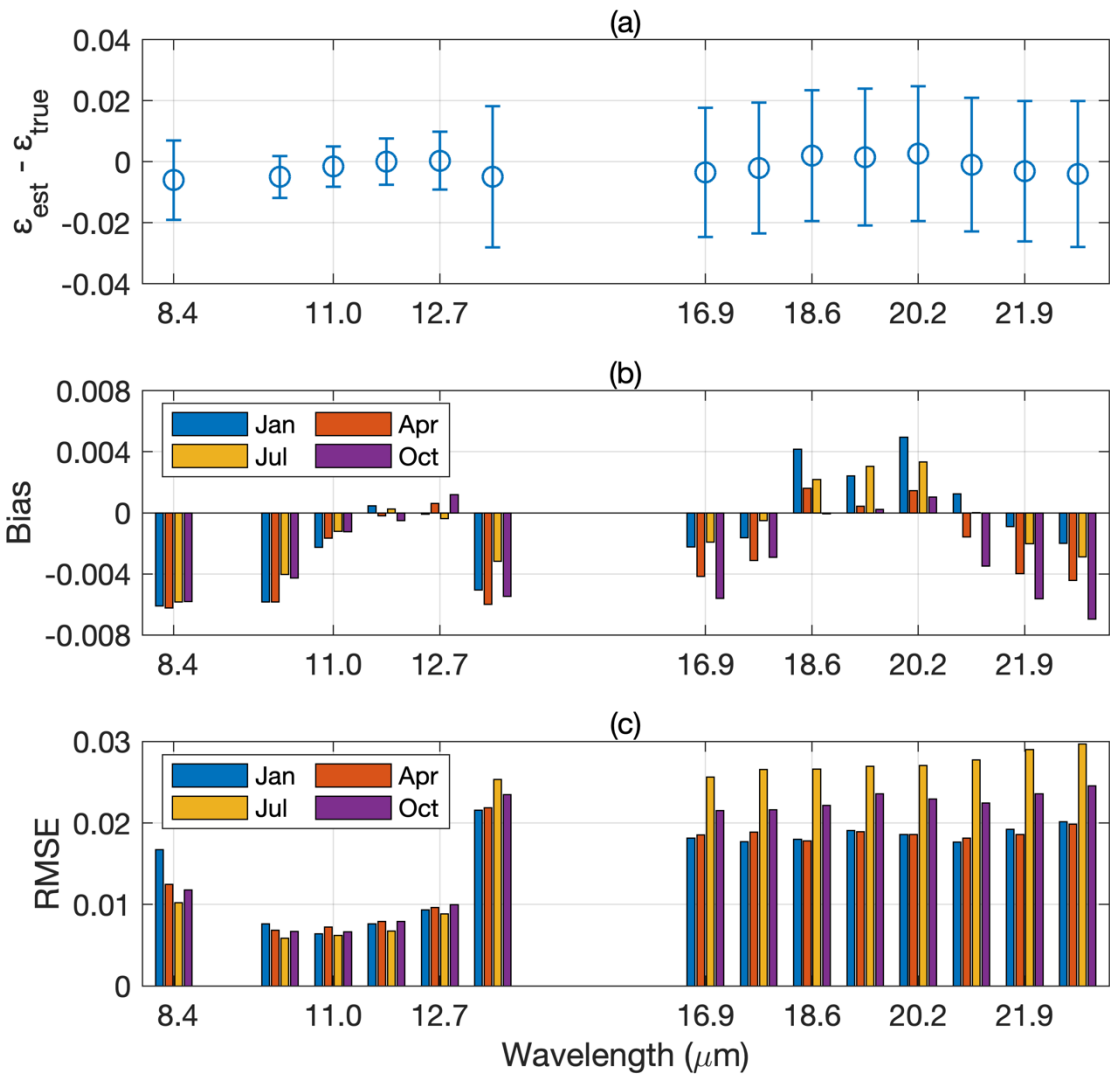


Figure 8. Statistics of the surface emissivity retrievals over the Arctic (60-90°N, 0-360°E). (a) The mean bias (open circles) and the corresponding RMSE (vertical bars) based on all 960 cases. (b) The mean bias for January, April, July, and October cases, respectively. Each month has 240 cases. (c) The RMSE for January, April, July, and October cases, respectively.

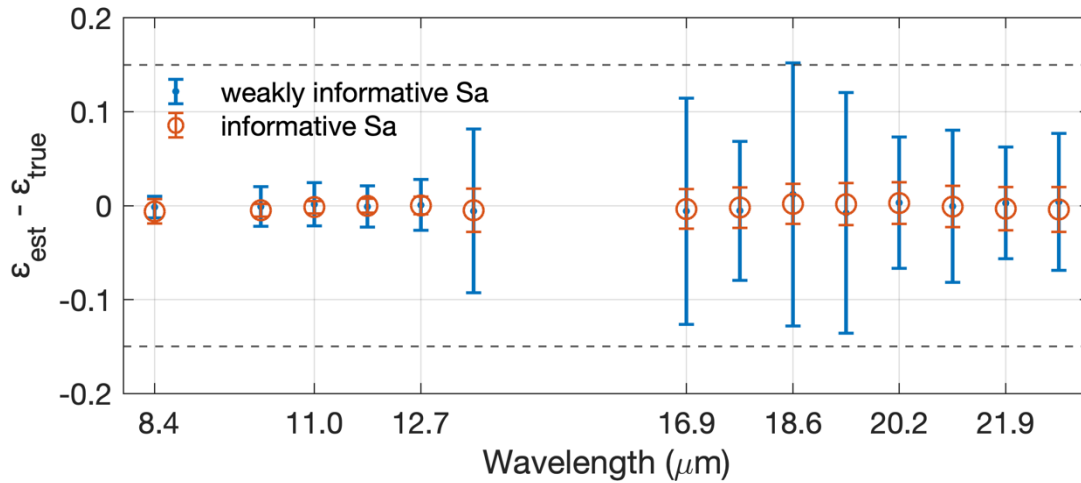


Figure 9. Blue lines with dots show the mean biases and the RMSEs of surface spectral emissivity retrievals using a weakly informative *a priori* covariance matrix (a diagonal matrix with the same value of 0.15^2 on its diagonal). Orange line with open circle denotes the counterparts from using the *a priori* covariance matrix shown in Figure 2, which is denoted as informative \mathbf{S}_a . For comparison, dashed lines denote the ± 0.15 threshold (i.e., *a priori* uncertainty for weakly informative \mathbf{S}_a).